The Two-Photon Exchange Contribution to Electron-Neutron Elastic Scattering in Hall A at Jefferson National Lab
Dissertation Proposal

Sebastian Seeds
University of Connecticut
Department of Physics

(Dated: January 9, 2023)

World data describe a significant discrepancy between the proton electric to magnetic Form Factor Ratio (FFR) G_E/G_M as measured by polarization transfer methods and the proton FFR as measured using the Rosenbluth method. Emergence of this discrepancy gave rise to what's currently known in the literature as the Form Factor Ratio Puzzle (FFRP). In the neutron Two-Photon Exchange (nTPE) experiment which ran in January of 2022, we made a relatively high precision measurement of the electron-neutron electron-proton cross section ratio $\sigma_{e-n}/\sigma_{e-p}$ at two different values of the virtual photon polarization ϵ. Measurements at these two polarization points allow for the extraction of the ratio of longitudinally polarized to transversely polarized virtual photon cross-sections σ_L/σ_T, or the Rosenbluth Slope (RS), expected to be linear in One-Photon Exchange (OPE), but non-linear with hard Two-Photon Exchange (TPE) contributions to the elastic nucleon scattering cross section. By measuring $\sigma_{e-n}/\sigma_{e-p}$, we employed the so-called "ratio" method to minimize systematic error such that we are able to measure the neutron FFR discrepancy with enough precision to effectively distinguish between competing models of the TPE contribution to the neutron FFR at four-momentum transfer $Q^2 = 4.5\ (GeV/c)^2$.

I. INTRODUCTION

In the Born approximation for electron-nucleon (e-N) scattering, the interaction is mediated by a single photon (OPE). In this approximation, the e-N elastic cross section can be parameterized by Sachs form factors (G_E for electric and G_M for magnetic):

$$\left(\frac{d\sigma}{d\Omega}\right)_{eN\to eN} = \frac{\sigma_{Mott}}{\epsilon(1-\tau)}\left[\tau\cdot G_M^2(Q^2) + \epsilon\cdot G_E^2(Q^2)\right] \tag{1}$$

Here the Mott cross section (σ_{Mott}) considers only point like Coulombic and magnetic interactions between electron and neutron, $\tau \equiv -q^2/4M^2$ (M neutron mass), $Q^2 \equiv -q^2 \equiv 4EE'\sin^2\theta/2$ (θ electron scattering angle, E beam energy, E' scattered electron energy), and $\epsilon \equiv 1/(1+2(1+\tau)\tan\theta/2)$ is the longitudinal polarization of the virtual photon.

One can reduce this differential cross section through further parameterization, where:

$$\sigma_r \equiv \left(\frac{d\sigma}{d\Omega}\right)\cdot\frac{\epsilon(1+\tau)}{\sigma_{Mott}} \tag{2}$$

We obtain the reduced cross section (σ_r):

$$\sigma_r = \tau\cdot G_M^2(Q^2) + \epsilon\cdot G_E^2(Q^2) = \sigma_T + \epsilon\cdot\sigma_L \tag{3}$$

Here $\sigma_T(\sigma_L)$ is the transversely(longitudinally) polarized virtual photon cross section. In OPE, the cross section is the reduced cross section - linear in ϵ. The RS, modulo correction factors in OPE, is the ratio of longitudinal to transverse virtual photon polarization (σ_L/σ_T). Figure one demonstrates the well-known and large discrepancy between the measured RS and expected OPE value for the proton at Q^2 =4.5 $(GeV/c)^2$.

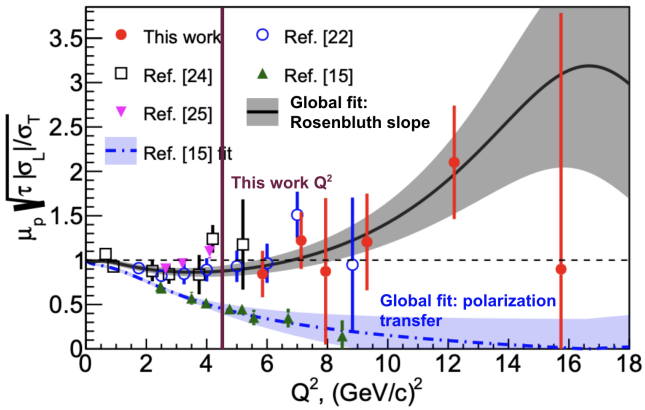

FIG. 1. Square root of Rosenbluth slope with corrections for $\sqrt{\tau}$ and μ_p. Plot references from R3 with some edits.

Measurements of nucleon form factors can be experimentally obtained via two methods. The first is the Rosenbluth method, which is employed for nTPE (detailed in section II.C). The second is the polarization transfer method and measures the azimuthal polarization asymmetry resulting from polarization transfer from longitudinally polarized electrons to the recoiling nucleon or from a polarized electron beam and polarized target. Because these polarization transfer measurements are directly sensitive to the ratio G_E/G_M and insensitive to TPE contributions to cross section measurements, they serve as a baseline to compare Rosenbluth method data to OPE expectations.

The RS in OPE is related to the ratio of the electromagnetic form factors:

$$\sqrt{\tau \cdot RS} = \sqrt{\frac{\tau|\sigma_L|}{\sigma_T}} = \frac{G_E}{G_M} \tag{4}$$

Each of these form factors describe the internal structure and quark distribution of the nucleon and depend only on Q^2. Perturbative Quantum Chromodynamics (pQCD) predicts the behavior of G_M and G_E, but it isn't yet clear over what Q^2 range pQCD scaling is valid. It is clear via world data that these form factors begin to behave differently for the proton starting at $Q^2 = 1$ $(GeV/c)^2$. As such, we expect to see a significant difference in the σ_L/σ_T ratio between nTPE data and OPE expectations for Q^2 greater than 1 $(GeV/c)^2$ for the neutron. By extracting the RS which depends on σ_L and σ_T at $Q^2 = 4.5$ $(GeV/c)^2$, we will measure the TPE contribution to neutron electromagnetic form factors in this higher Q^2 region.

II. EXPERIMENTAL CONTEXT

A. Background Theory and Motivation

Foundational experiments conducted in the 1950s by R. Hofstadter showed that nucleons have a substructure. Because electrons are insensitive to the strong force, one is able to probe the electromagnetic properties of this substructure to determine their hadronic current via electron scattering experiments. Today, these properties for hadrons (assuming OPE) are captured by the Dirac and Pauli form factors, F_1 and F_2 respectively. F_1 is helicity-conserving and describes the distribution of electric charge in the hadron and F_2 describes the distribution of the magnetic moment in the hadron. Together F_1 and F_2 constitute the hadronic current. *These measures constitute fundamental physical properties worthy of inquiry in their own right.* The Dirac and Pauli form factors are related to the aforementioned Sachs form factors thus:

$$F_1 = \frac{G_E + \tau G_M}{1+\tau} \quad ; \quad F_2 = \frac{G_M - G_E}{\kappa(1+\tau)} \tag{5}$$

Here κ is the anomalous magnetic moment of the nucleon.

In terms of generalized parton distributions (GPDs), these form factors are the first moments of GPDs which are functions of Bjorken x (x), reaction "skewdness" (ξ), four-momentum transfer by the electron (t), and the Q^2 evolution scaling (μ).

$$F_1(t) = \sum_q \int_0^1 H^q(x,\xi,t,\mu)dx \tag{6}$$

$$F_2(t) = \sum_q \int_0^1 E^q(x,\xi,t,\mu)dx \tag{7}$$

Each of H^q and E^q (the GPDs) are summed over all quarks and anti-quarks. Experiments that measure GPDs directly, like deeply virtual Compton scattering (DVCS), are scarce and don't exist for high Q^2 at present. Instead, attempts to parameterize GPDs are underway which rely heavily on electromagnetic form factors (F_1 and F_2) and parton distributions provided by deep inelastic scattering (DIS) experiments. The FFRP indicates that OPE assumptions are insufficient at higher Q^2 and that Radiative Corrections (RC) must play a significant role in that region. While the most recent analysis of non-TPE RC reduces the RS and narrows the discrepancy, it confirms the FFRP nonetheless, indicating that TPE is the most likely explanation of the discrepancy. In short, to better understand parameterization of GPDs with electromagnetic form factors, the extant to which TPE contributes to electron-hadron scattering will first need to be understood.

B. Previous Measurements

Measurements done by R. Hofstadter supported the OPE approximation in e-p scattering by showing a linear dependence of σ_r to ϵ. Later tests of linearity up to $Q^2 = 3$ $(GeV/c)^2$ indicate that form factors follow the dipole form:

$$G_D \equiv \frac{1}{\left(1+\frac{Q^2}{\Lambda^2}\right)^2} \quad ; \quad \Lambda = 0.71(GeV/c)^2 \tag{8}$$

This indicates that $\mu_p G_E/G_M \approx 1$ over Q^2 and consequently the OPE approximation was applied to extract form factors at higher Q^2 via elastic cross section analysis under the assumption that $RS \approx 1$. These data confirmed the pQCD predicted Q^2 independence of G_M above $Q^2 = 10$ $(GeV/c)^2$.

However, at higher Q^2, τ enhances the contribution of G_M (equation 3) and the use of the Rosenbluth method and cross-section measurements to extract G_E becomes difficult. As a result, double polarization experiments were developed along with the OPE formalism to access the FFR directly, independent of the individual form factors. These Jefferson Lab measurements revealed that the FFR extracted from these experiments decreased largely with Q^2 as compared to the FFR extractions via cross-section measurements. This discrepancy gave rise to the FFRP as it is known today.

Further analysis of proton cross-section world data and higher-precision measurements employing the Rosenbluth method were performed and confirmed the linearity of the RS for the proton up to $Q^2 = 5.5$ $(GeV/c)^2$. With corrections for TPE, these data helped to confirm the TPE solution for the FFRP (see figure 2). Later, $e^{\pm}$-p scattering experiments measured TPE contributions to e-p cross sections up to $Q^2 = 2$ $(GeV/c)^2$.

In the case of the neutron, few e-n scattering measurements exist to inform the FFRP. In the 1960s and 1970s

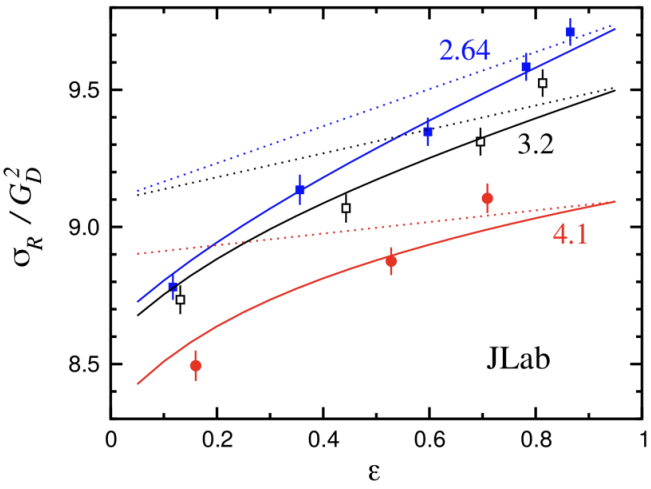

FIG. 2. Data employing the Rosenbluth method measuring the reduced cross-section of the proton. The dotted fit lines are from data employing polarization transfer methods. The solid fit lines are the same, but with TPE corrections.

measurements by Bartel et al. were conducted and represent the highest precision achieved in measurements of neutron form factors (see figure 3). These measurements lack sufficient precision to measure the RS.

C. Rosenbluth Method

The Rosenbluth method (also known as the Rosenbluth technique or L/T separation) is an experimental technique used to separate G_E and G_M based on the assumed linear dependence of G_E on ϵ (equation 1). This assumed linearity is commensurate with the OPE approximation. By holding Q^2 fixed and varying the electron scattering angle θ, one can construct the linear system:

$$y(\epsilon) = \sigma_r(\epsilon) = \tau \cdot G_M^2 + \epsilon \cdot G_E^2 \tag{9}$$

With two points on the line, the y-intercept represents $\tau \cdot G_M^2$ and the slope of y represents G_E^2 (see figure 4). In this construction, $y(\epsilon)$ can be measured:

$$y(\epsilon) = \frac{\epsilon(1-\tau)}{\sigma_{Mott}} \cdot \left(\frac{d\sigma}{d\Omega}\right)_{eN \to eN} \tag{10}$$

Here the cross-section is measured and the other variables vary by kinematic. In an equivalent form, the Rosenbluth method can be seen to be equivalent to L/T separation, and so it is often referred to as such in the literature (equation 3).

This work will employ the Rosenbluth method, assuming linearity of G_E on ϵ, to make a precision measurement of the RS at $Q^2 = 4.5\ (GeV/c)^2$. This value will be compared to polarization transfer world data to measure the TPE contribution to the RS.

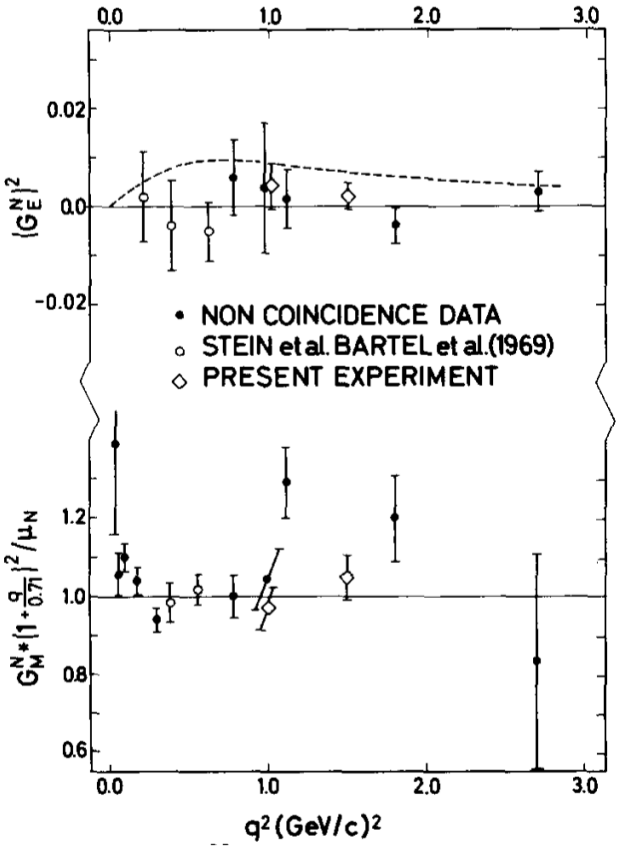

FIG. 3. Most recent elastic e-n scattering measurements up to $Q^2 = 3\ (GeV/c)^2$ conducted by Bartlet et al. over 50 years ago. Such measurements are insufficient to extract the Rosenbluth slope.

III. INSTRUMENTATION

A. Measurement Technique

Due to the lack of a free neutron target, measurements of the TPE contribution to the neutron are difficult to obtain. Using a liquid deuterium (LD2) target presents the best option due to the loose coupling between the single proton and single neutron in the nucleus. Measurements of the neutron's magnetic form factor (G_M^n) have been taken using LD2 with an evolution of experimental methods. The first relies on the subtraction of the proton quasi-elastic D(e,e'p) cross section and is fraught with systematic uncertainties arising from inelastic and secondary scattering contamination. The second, and more relevant here, is the so-called "ratio-method" or "Durand technique", so named for L. Durand who first proposed it. This method relies on the simultaneous measurement of the quasi-elastic D(e,e'p) proton and the quasi-elastic D(e,e'n) neutron to obtain the quasielastic nucleon cross-section ratio. In this ratio, many of the prominent systematic errors cancel. We will employ the ratio method

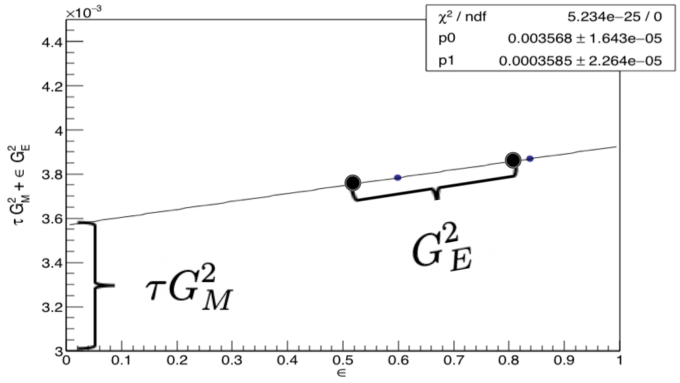

FIG. 4. Assuming linearity in ϵ, one can extract the Sachs form factors with a precision measurement of the nucleon cross-section.

to extract the RS in nTPE.

We will obtain G_E^n via the Rosenbluth technique with the ratio ($R_{n/p}$) of quasi-elastic yields ($N_{e,e'n}$ for quasi-elastic neutron and $N_{e,e'p}$ for quasi-elastic proton) thus:

$$R_{n/p} \equiv R_{observed} = \frac{N_{e,e'n}}{N_{e,e'p}} \tag{11}$$

These yields are the experimental observables. This observed ratio ($R_{observed}$) must be corrected with a factor that accounts for hadron detection efficiencies, RC, absorption effects from the target to the detector through the air, and re-scattering effects. This correction (f_{corr}) is applied thus:

$$R_{corrected} = f_{corr} \times R_{observed} \tag{12}$$

The aggregate experimental observable A is the ratio of $R_{corrected}$ for two values of ϵ (differing between SBS8 and SBS9):

$$A = \frac{R_{corrected,\epsilon_1}}{R_{corrected,\epsilon_2}} \tag{13}$$

$R_{corrected}$ can be related to the measured cross sections thus, where $RS^N = \sigma_L^N/\sigma_T^N$:

$$R_{corrected} = \frac{\sigma^n_{Mott}(1+\tau_p)}{\sigma^p_{Mott}(1+\tau_n)} \times \frac{\sigma^n_T + \epsilon\sigma^n_L}{\sigma^p_T + \epsilon\sigma^p_L} \tag{14}$$

$$= \frac{\sigma^n_{Mott}(1+\tau_p)}{\sigma^p_{Mott}(1+\tau_n)} \times \frac{\sigma^n_T}{\sigma^p_T} \times \frac{1+\epsilon RS^N}{1+\epsilon RS^N} \tag{15}$$

Defining the first term as the Mott ratio:

$$R_{Mott} = \frac{\sigma^n_{Mott}(1+\tau_p)}{\sigma^p_{Mott}(1+\tau_n)} \tag{16}$$

..the aggregate observable A becomes:

$$A = \frac{R_{Mott,\epsilon_1}}{R_{Mott,\epsilon_2}} \times \frac{1+\epsilon_1 RS^N}{1+\epsilon_2 RS^N} \times \frac{1+\epsilon_2 RS^P}{1+\epsilon_1 RS^P} \tag{17}$$

Now we may define a term B which depends only on the proton RS:

$$B = \frac{R_{Mott,\epsilon_1}}{R_{Mott,\epsilon_2}} \times \frac{1+\epsilon_2 RS^P}{1+\epsilon_1 RS^P} \tag{18}$$

Notably R_{Mott} can be determined to very high accuracy at our kinematics and RS^P is well known from world data ($RS^P = 0.107 \pm 0.010$). Taking advantage of the this and Taylor expanding we can write A in terms of B:

$$A = B \times \frac{1+\epsilon_1 RS^N}{1+\epsilon_2 RS^N} \tag{19}$$

$$\approx B\big(1 + RS^N(\epsilon_1 - \epsilon_2)\big) \tag{20}$$

Solving for RS^N where $\Delta\epsilon = \epsilon_1 - \epsilon_2$ gives the most suggestive form of the Rosenbluth slope for the neutron:

$$RS^N = \frac{A - B}{B\Delta\epsilon} \tag{21}$$

We will determine B from global data and we will measure A using the Mott cross sections and via the quasi-elastic neutron to proton yield ratio.

B. CEBAF

CEBAF stands for the Continuous Electron Beam Accelerator Facility, now known as Jefferson Lab, and is located in Newport News, Virginia. It consists of two parallel linear accelerators (linacs) connected by recirculation arcs on either side designed to bend electrons from one linac to the other, an electron injector, and several experimental halls. Each linac is comprised of several cryomodules containing superconducting Niobium cavities which resonate in radio frequencies (SRF cavities). Niobium superconducts in superfluid Helium, at around 2 K, which reduces the heat load generated by the cavities by a factor of 3 and improves efficiency. After the 12 GeV upgrade, there are now 52 and 1/4 cryomodules with eight SRF cavities per cryomodule operating in both linacs. Each linac is capable of imparting 1090 MeV to electrons moving through it which are kept on track by several arcs of magnets that can handle the high momentum of 12 GeV electrons. Figure 5 depicts CEBAF.

The accelerator is capable of delivering polarized or unpolarized electrons as produced in the injector. This production results from near infrared laser light impinging on Gallium Arsenide photocathodes under a high negative potential designed to repel electrons produced via the photoelectric effect into the accelerator. These electrons are effectively continuous wave (CW), but are in fact delivered to the experimental halls in bunches separated by 4 ns. CEBAF is the only electron beam delivery mechanism used in nTPE.

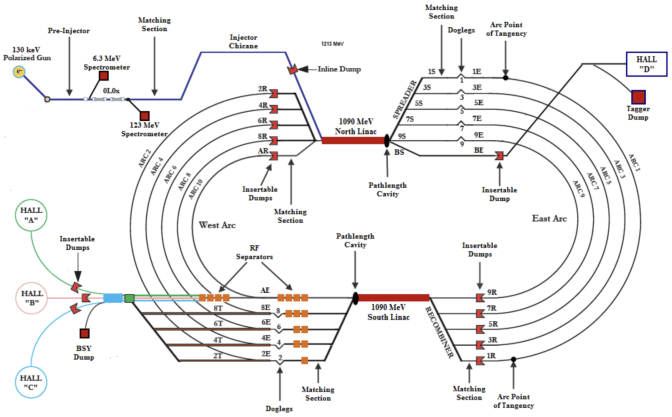

FIG. 5. Schematic of CEBAF after the 12 GeV Upgrade

TABLE I. nTPE Kinematics

Point	Q^2 (GeV^2)	E (GeV)	E' (GeV)	θ_{BB}	θ_{SBS}	ϵ
SBS9	4.5	4.03	1.63	49	22	0.523
SBS8	4.5	5.97	3.59	16.5	29.4	0.915

C. Hall Layout and Kinematics

In order to measure nTPE, detailed measurements of the momentum, energy, and position of outgoing electrons and hadrons resulting from quasi-elastic D(e,e'n) and D(e,e'p) collisions at a single Q^2 ($4.5\ GeV^2$) are necessary. Two spectrometers are deployed for this task; the Hadronic Calorimeter (HCal) to measure scattered protons and neutrons and the BigBite (BB) Spectrometer to measure scattered electrons. Figure 6 depicts both spectrometers in relation to the beamline and scattering chamber. With Q^2 fixed, the two positions of the spectrometers (θ) allow us to vary the virtual photon polarization ϵ, necessary to extract the RS (M_n is the mass of the neutron).

$$\epsilon = 1/\left(1 + 2\left(1 + \frac{Q^2}{4M_n^2}\right)\tan^2(\theta/2)\right) \tag{22}$$

The measured kinematics are in Table I.

D. BigBite Spectrometer

The purpose of the BigBite spectrometer is to measure the position and momentum of scattered electrons. Its namesake comes from the large momentum bite that it can sample, ± 10 % of the central momentum of the scattered electron. With precision e' position over several planes and subsystems and precise e' momentum per event, e' tracks can be reconstructed back to the target vertex location from many possible combinations. These tracks provide the means to calculate kinematical quantities for scattered protons and neutrons and enable tight cuts on invariant mass (W) and reconstructed scattered nucleon position. With these cuts, one can select elastic events (via LH2) and quasi-elastic events (via LD2) in the hadron arm (Section E). These cuts are essential at $Q^2 = 4.5\ GeV^2$ due to the reduced elastic and quasi-elastic proton and neutron cross sections at this relatively high momentum transfer and coincident high background rates in all detectors.

The BigBite spectrometer is made of five subsystems. In alphabetical order: the BigBite Calorimeter (BBCal), the BigBite magnet, the Gas Electron Multipliers (GEMs), the Gas Ring ImagiNg CHerenkov detector (GRINCH), and the Hodoscope. Figure 7 depicts the BigBite spectrometer stack.

1. *BBCal*

The BigBite Calorimeter is a lead glass electron Calorimeter designed to measure the energy of electrons moving through it. It is divided into two planes, the preshower (PS) and shower (SH), with the former coming first proceeding outward from the scattering chamber and target. The PS has 52 blocks, stacked in a 26 row by 2 column grid with their long dimension perpendicular to the the beam. The SH has 189 blocks, stacked in a 27 row by 7 column grid with the same long-dimension orientation as PS. Each of these blocks is coupled to a photomultiplier tube (PMT) read out by flash analog to digital converters (fADCs). Between both BBCal planes, all of the electron energy for events of interest is sampled such that it provides a backstop for elastic and quasielastic events of interest. Via cuts on the energy deposited in the PS, pions can be rejected during analysis. The final energy resolution of BBCal is still being evaluated, but initial estimates place it at 5.9 %(7.8 %) for SBS9(SBS8).

Analog sums over these blocks which pass threshold constitutes the main single-arm trigger for the experiment. This threshold is remotely configurable and tuned to ensure the event trigger rate does not significantly reduce the live time of the data acquisition (DAQ) and the trigger rate is kept $< 5\ kHz$.

2. *BigBite Magnet*

The purpose of the BigBite magnet is to bend charged particles into different trajectories to enable momentum selections on scattered electrons in the BigBite spectrometer. It is a dipole magnet which produces a roughly 1.2 T magnetic field.

3. *GEMs*

GEMs are charged particle tracking detectors which consist of several polymer foils with a high density of small holes (tens of μm diameter). These foils are separated by order mm distances forming cells, each cell

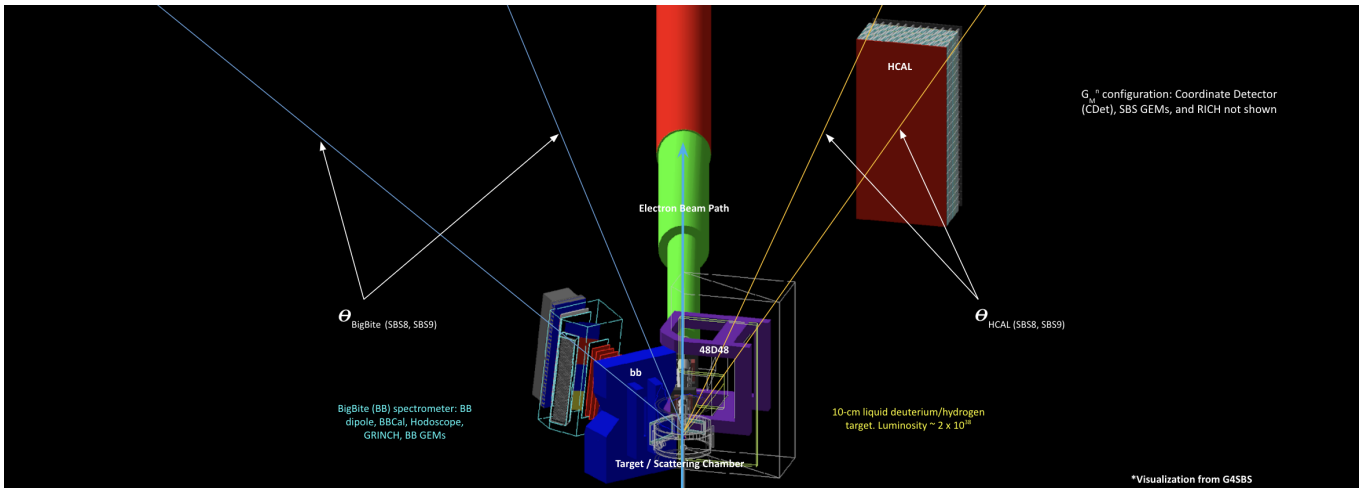

FIG. 6. Simulated Layout of the SBS Spectrometer in Experimental Hall A, Jefferson Lab

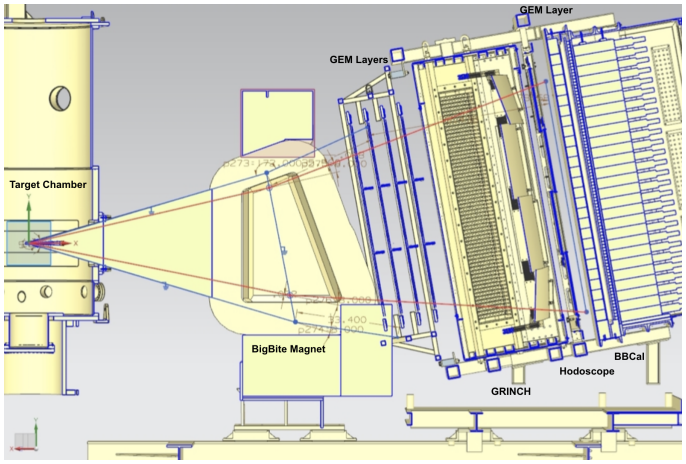

FIG. 7. Schematic of the BigBite Spectrometer, Side View

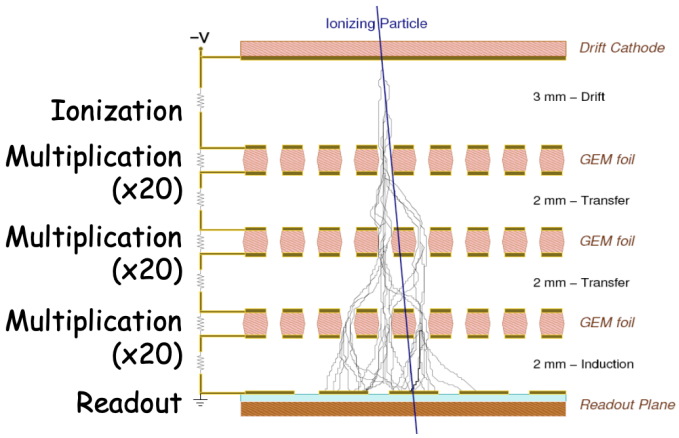

FIG. 8. Slice of one GEM Depicting Ionization Event Over Several Foils

is filled with 75%/25% $Argon/CO^2$, and each cell is placed under a strong potential (roughly 4 kV). When a charged particle passes through the detector it ionizes many molecules of the heavy gas producing free electrons which avalanche via many collisions producing additional ionized electrons and are converted at the readout plane to signal read out by APVs (many-channel analog to digital converters). Figure 8 depicts one such event on a single GEM. Via COMPASS results, GEMs are capable at event rates as high as 25 kHz/mm^2. Expected position resolution 70 μm. With digitized monte-carlo data (via G4SBS) tracking efficiency with current algorithms 60-80%. Final detector performance will be evaluated during analysis of GMn data.

nTPE used GEMs developed by the University of Virginia (UVA) which consist of several cell strips oriented $\pm$ 30 deg (u/v) with respect to the transverse direction. These strips cover an active area of 40 x 150 cm^2 with very high segmentation (64k readout channels). For nTPE, UVA GEMs constituted all of the five GEM layers used for e' track reconstruction.

4. *GRINCH*

GRINCH is designed to provide offline particle identification (PID), specifically for pion rejection. It consists of a 88.9 cm deep tank filled with heavy gas containing four cylindrical mirrors. As charged particles pass into the heavy gas (C_4F_8), they emit cherenkov light which these mirrors focus onto an array of 510 PMTs. Each of these PMT signals is processed by a front end (FE) NINO card imposing an analog threshold. Surviving analog PMT signals are read out by a dedicated VETROC TDC channel recording leading edge (LE), trailing edge (TE), and time over threshold (TOT) information.

Due to the staggered design of the PMT array and segmentation, cherenkov rings can be resolved for electrons and pions, with the latter capable of rejection due to the discernible effect of much higher pion momentum on the

cherenkov angle (θ_c) and consequent ring size.

While the PID functionality of GRINCH isn't necessary for nTPE, it provides another track-finding constraint to reduce the combinatorics evaluated during replay of data.

5. *Hodoscope*

The hodoscope consists of 90 scintillator bars arranged perpendicular to the dispersive direction in the BigBite stack and are read out by a PMT on each end. Each of these PMTs is read out by a CAEN 1190 TDC which records LE and TE information with high precision. This requires a similar setup as the GRINCH, where analog signals from PMTs are processed by FE NINO cards which apply a threshold for good hits before sending passing signals to TDC channels. Due to this high timing precision, the hodoscope provides the event reference time for timing signals used in other detectors, especially the HCal and its associated time of flight (TOF) measurement for scattered elastic and quasielastic nucleons.

With accelerator RF corrections, timing resolution of 200 ps is expected, with actual performance to be determined during analysis of GMn data. While the segmentation of the hodoscope is low relative to the GEMs, it also provides additional position constraints on good e' tracks in the electron arm.

E. Hadron Arm Spectrometer

The hadron arm spectrometer consists of the SBS magnet and HCal and detects recoil elastic and quasielastic nucleons. With e' track information from the BigBite spectrometer, the q vector for recoil nucleons can be obtained and applied to constrain a search region on HCal for quasielastic e-p and e-n nucleons. Without detection of the spectator nucleon in D(e,e'n)p and D(e,e'p)n events, separation of protons and neutrons in the SBS magnetic field is necessary. Where X is the dispersive direction, Figure 9 depicts the separation of quasielastic nucleons depending on charge as measured in HCal during the experimental running.

1. *SBS Magnet*

The SBS dipole magnet operates at a maximum of 2100 A producing a 1.7 $T\dot{m}$ magnetic field integral. This magnetic field bends the trajectory of scattered quasielastic protons from LD2 and elastic protons from LH2 and provides the only means of separating scattered neutrons and protons. The field volume accommodates and matches the full acceptance of HCal and will sweep charged background particles of energy $< 1.3\ GeV$ out of the acceptance. From Monte Carlo simulations, charged

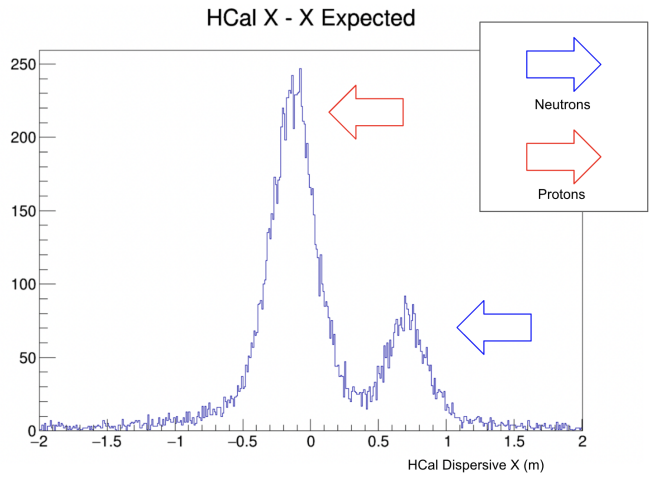

FIG. 9. Difference of HCal Cluster Center and Projected Position from e' Over Dispersive Direction X (m)

quasielastic contamination from charged particles is expected to be negligible.

2. *HCal*

The 40-ton hadronic calorimeter is located on beam right facing downstream from the scattering chamber and will measure energies, position, and timing of scattered hadrons (protons and neutrons) for nTPE and all SBS experiments. HCal consists of 288 individual showering modules designed to produce electromagnetic showers from scattered nucleons and sample the energy of those showers. The light gathered from these reactions is collected by a PMT on each channel whose signals are read out via flash analog to digital converters (fADCs) and multi-hit time to digital converters (F1TDCs). A single module consists of stacked scintillator and iron absorbers coupled to a wavelength shifter designed to match scintillated light to the optimal wavelength of the coupled Photonis XP2262 and XP2282 photomultiplier tubes (PMTs). In front of the entire acceptance is a 0.75 inch steel plate which reduces interactions from low energy secondaries and assists in the creation of electromagnetic showers.

Precise position resolution is necessary for proton and neutron cross section calculations. Simulated position resolution expectations are shown in Figure 10. Initial data from GMn show that these expectations are met, but will be further confirmed during analysis.

In order for the Durand technique to effectively cancel systematic uncertainties, the detection uniformity across HCal must remain roughly constant across the acceptance and the detection efficiency must be near unity for all measured nucleon momenta. To spec, HCal is expected to display uniform detection efficiency across its acceptance. Figure 11 depicts the first estimates of detec-

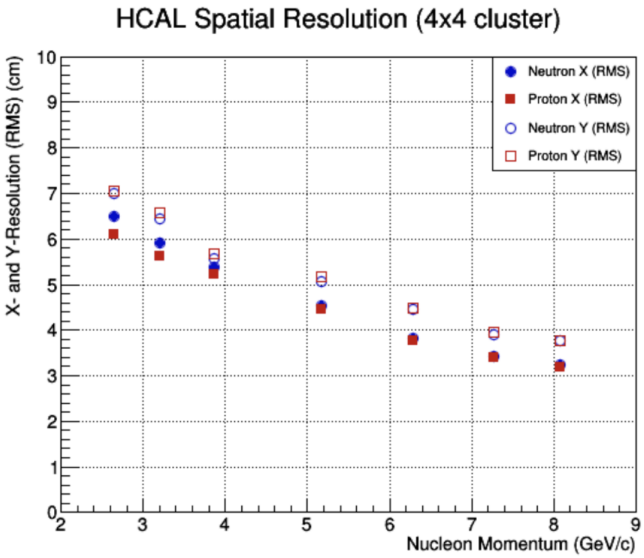

FIG. 10. HCal Position Resolution via G4SBS (Geant 4 for SBS) Simulations

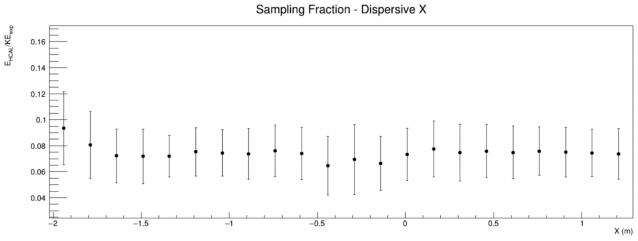

FIG. 11. HCal Sampling Fraction vs Dispersive Direction X, SBS8

tion uniformity from GMn data. Figure 12 shows simulated expectations for detection efficiency for all relevant nucleon momenta.

Simulated timing resolution is expected to be better than 1 ns. Energy resolution is expected to be roughly 60% of incident nucleon energy which is more than sufficient for nTPE.

F. Front End (FE) and Data Acquisition (DAQ)

For both the BigBite spectrometer and Hadron arm spectrometer, analog signals are processed through many NIM analog sum and logic modules used to clean backgrounds via thresholds and produce triggers. All FE NIM electronics are radiation hard and purely analog enabling closer proximity to the spectrometers and very high rate processing. Two FE areas exist, one for the HCal located on the HCal mezzanine behind the bulk of the detector and one for the BigBite arm located behind the BigBite detector stack, with each sending all signals to the DAQ

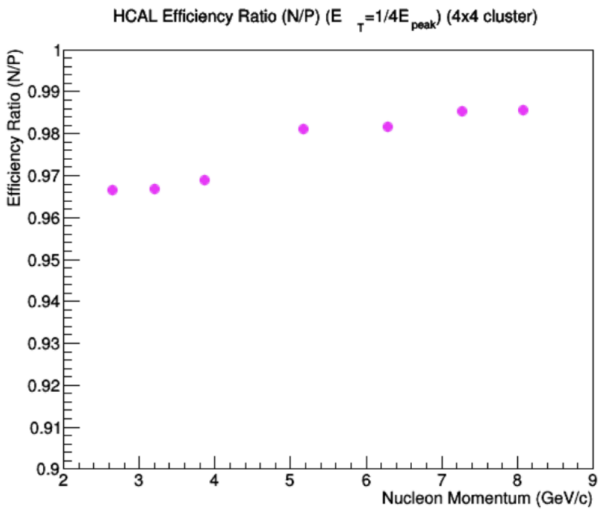

FIG. 12. HCal Detection Efficiency, G4SBS

bunker located upstream from the target chamber beam left with respect to downstream. For nTPE and GMn the single arm event trigger is formed in the FE as a sum of shower and preshower blocks over threshold in BBCal. Analog signals are digitized in the DAQ bunker with fADCs and TDCs located there. Additionally, the event trigger is formed here with the trigger supervisor (TS) digitized data is encoded and recorded with CEBAF Online Data Acquisition (CODA).

For brevity the high complexity of the FE cable maps, FE logic, DAQ encoding, and DAQ structure are left out of this proposal.

G. Detector Calibrations

Calibrations currently underway after experimental running fall broadly under the categories of timing and energy. In the energy set, each of the subsystems which employ avalanche photomultipliers (PMTs and GEMs) must, at minimum, gain match across channels and, for the calorimeters, provide gain coefficients to convert ADC signals to energy in GeV. In the timing set, those that employ TDCs must also correct for signals considering detector geometry, data acquisition effects (ie. time-walk), and electronics jitter.

Along with detector-specific and beam-specific figures, all time and energy calibration parameters are passed to the SBS data decoding and replay software (Hall A analyzer and SBS-offline, respectively) which populates output data tree files with many sorted branches over events. These "cooked" data files are used for analysis. Details of these calibration efforts by subsystem and architecture of analysis files provided by SBS-offline are left out of this proposal for brevity.

IV. PROJECTIONS

A. Measurements and Rates

As shown in section II, measurement of the RS requires simultaneous proton and neutron yield measurements over two kinematics for SBS8 and SBS9. Both of these kinematics have been evaluated to meet expected uncertainties considering the largest expected systematic errors and projected statistics from the quasielastic counting rate before approval of the experiment. Owing to cancellation of many of the systematic errors which are a problem for absolute cross section measurements, foremost among the expected systematic errors in nTPE is inelastic contamination of the quasielastic proton and neutron yield.

To predict inelastic contamination, simulations where all particles from scattering events, including true quasielastic events, can be tracked were produced. These simulations depict the relative rates of quasielastic events and inelastics against both the center of mass energy (W):

$$W^2 = M_N^2 + 2M_N^2(E - E') - Q^2 \tag{23}$$

..and missing transverse momentum ($p_{\perp miss}$):

$$p_{\perp miss} = \sqrt{(q_x - p'_x)^2 + (q_y - p'_y)^2} \tag{24}$$

Results of these simulations show that judicious cuts on these quantities can reduce the inelastic contamination to less than 1 %. Figures 13 and 14 show the results of these simulations.

In principle, additional cuts can be placed to reduce inelastic contamination further including (but not limited to):

- Pion rejection in the electron arm via preshower energy threshold
- Vertex position of e' tracks back to within the bulk of the target
- E/p near unity after tracking calibration in the BigBite spectrometer
- Total energy deposited in BBCal
- Coincidence time between the BigBite single arm trigger and the HCal event
- Minimum GEM plane crossing threshold

Given these additional handles, the simulations provide a reasonable *upper* limit on inelastic contamination.

Accounting for detector efficiencies and acceptance, the quasielastic counting rate was also estimated via G4SBS simulations. For brevity, Table II shows the relative quasielastic yields assuming a running time $\Delta t = 12\ hours$, beam intensity of $I_{exp} = 30\ \mu A$, and LD2 target of length $l_{tgt} = 15\ cm$ and density $d_{tgt} = 0.169\ g.cm^{-3}$ without further details.

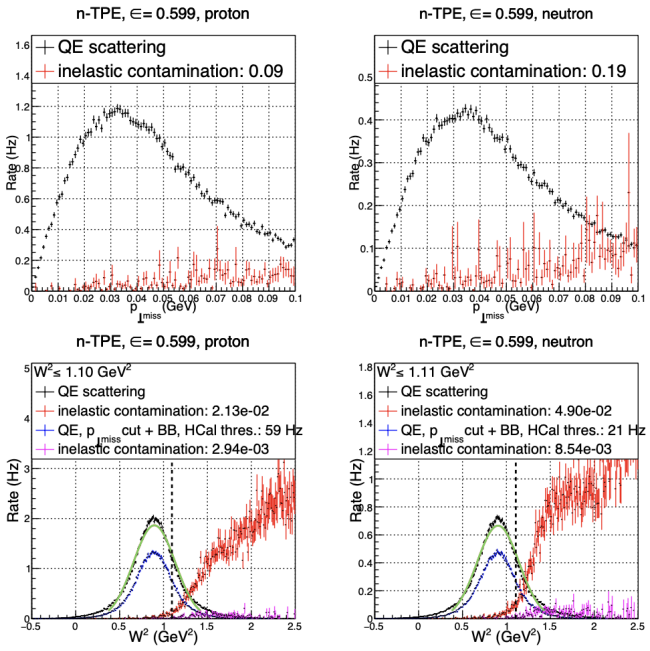

FIG. 13. Quasielastic and Inelastic SBS9 Distributions, Protons (left) and Neutrons (right), After W and $p_{\perp miss}$ Cuts

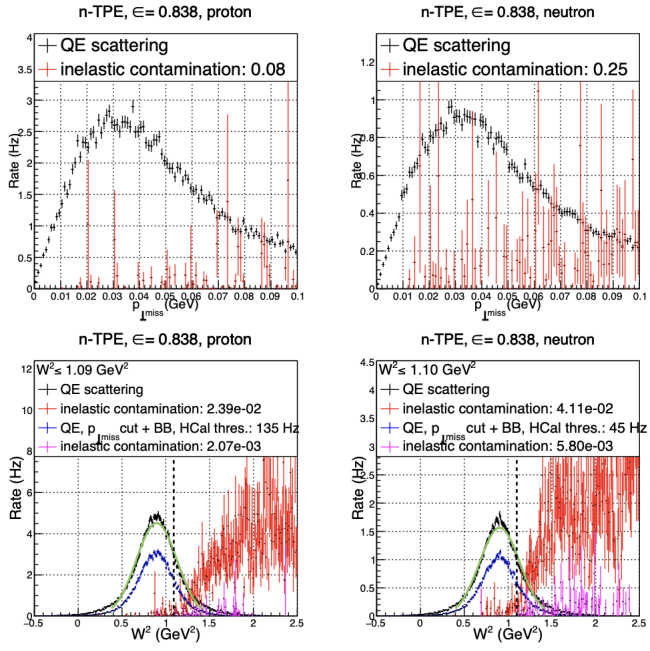

FIG. 14. Quasielastic and Inelastic SBS8 Distributions, Protons (left) and Neutrons (right), After W and $p_{\perp miss}$ Cuts

TABLE II. Expected Quasielastic (QE) Counting Rates

Kine	N_{QE} (e-n)	N_{QE} (e-p)
SBS9	9.07×10^5	2.55×10^6
SBS8	1.94×10^6	5.83×10^6

B. Systematic Error

As described in section III, the Durand technique enables cancellation of many systematic errors on the ratio $R = f_{corr} \times N_{e,e'n}/N_{e,e'p}$. These include (but aren't limited to):

- Nuclear corrections
- Accidentals
- Radiative corrections
- Target density

The significant sources of error that remain are acceptance losses, inelastic contamination, and nucleon misidentification.

Acceptance losses occur when BigBite detects a quasielastic electron, but the corresponding quasielastic proton or neutron from LD2 scatters outside of the acceptance of HCal. In principle, this effect will also cancel as long as the acceptance loss occurs in the same quantity between protons and neutrons, but due to the presence of the SBS field and detector geometry, a p-n acceptance asymmetry exists. With proper fiducial cuts during analysis, the effects of this asymmetry can be reduced, but systematic error remains (see Table III).

Inelastic contamination has been discussed in the previous section at some length. In short, simulations show that proper cuts on W and $p_{\perp miss}$ limit the contribution of inelastic contamination as the quadratic sum from proton and neutron from each kinematic to less than 1 % (see Table III).

Nucleon misidentification arises due to the long tail of the deuteron wave function which describes the probability that quasielastic protons will be scattered lower in the HCal acceptance and that quasielastic neutrons will be scattered higher in the HCal acceptance. Due to the larger quasielastic proton cross section and higher detection efficiency for protons in HCal, this will result in a larger proton contamination in the neutron peak and loss of protons in the proton peak than vice versa, and the relative errors do not cancel on the ratio. Using the farthest possible extent of proton and neutron contamination from the deuteron tail, the quasielastic proton and neutron yield from an uncontaminated area can be assessed. From this, the expected contamination rate can be calculated and subtracted from yields. With this technique, the "leakage" of protons into the neutron peak and vice versa can be measured to within 10 % and the corresponding error assessed (see Table III). Total combined error estimates can be found in Table IV.

TABLE III. Estimated Contributions to Systematic Error After Cancellation on Ratio $R = f_{corr} \times N_{e,e'n}/N_{e,e'p}$

Kine	SBS9	SBS8
Acceptance Losses	0.5 %	0.4 %
Inelastic Contamination	0.9 %	0.6 %
Nucleon Misidentification	0.6 %	0.6 %
Quadratic Sum of Above	1.3 %	1.0 %

TABLE IV. Total Estimated Systematic Error on RS, TPE

Systematic Uncertainty on Slope	± 0.01
Projected Systematic Uncertainty	± 0.01
$\mu n G_E^n/G_M^n = 0.55$	± 0.05
Combined uncertainty on TPE contribution to RS	**± 0.012**

V. PERSONAL WORK

The SBS series of experiments requires both the BigBite spectrometer and the Hadron Arm Spectrometer throughout. GMn and nTPE constitute a completely new set of detectors for Jefferson Lab and characterization, installation, commissioning, and calibration of all subsystems detailed in section III was planned and executed. Along with Dr. Scott Barcus, I led the hardware and software effort for HCal; supported the hardware for the BBCal, Hodoscope, GRINCH, and FE, and DAQ subsystems; and supported software development for BBCal and online data monitoring. I've also worked to support the preparation for other experiments through simulation development and RICH hardware work. Some explanation of this work follows, but details are left out for brevity.

A. Hardware

With Dr. Barcus, I managed and executed all hardware requirements for HCal testing and commissioning, save the movement of the 40 ton detector into the hall. This included all cabling, cable maps, FE single arm triggers and logic (cosmic, LED, and overlapping regions), FE thresholds, remote FE threshold control, FE amplification, FE crate power, HV cabling and control, PMT base measurement and installation, PMT optical coupling, LED programming, LED power control, LED optical fiber installation, signal time matching/delays, DAQ crate power and timing sync, DAQ remote power cycling, DAQ-side pulse shaping, fADC installation, F1TDC installation, fADC/F1TDC cabling/mapping, LED trigger veto, trigger timing, trigger supervisor (TS) inclusion, and other tasks. We expect to publish details of this work and the SBS HCal in a NIM paper after resolution and efficiency details can be determined throughout GMn/nTPE data analysis.

I was also involved in hardware installation efforts for all other subsystems. This included cable layout and installation, FE electronics, NINO diagnosis and testing, HV remote power cycling, optical cabling, DAQ timing synchronization, high resolution spectrometer (HRS) fADC replacement and addressing, and level one accept (L1A) trigger installation and delays.

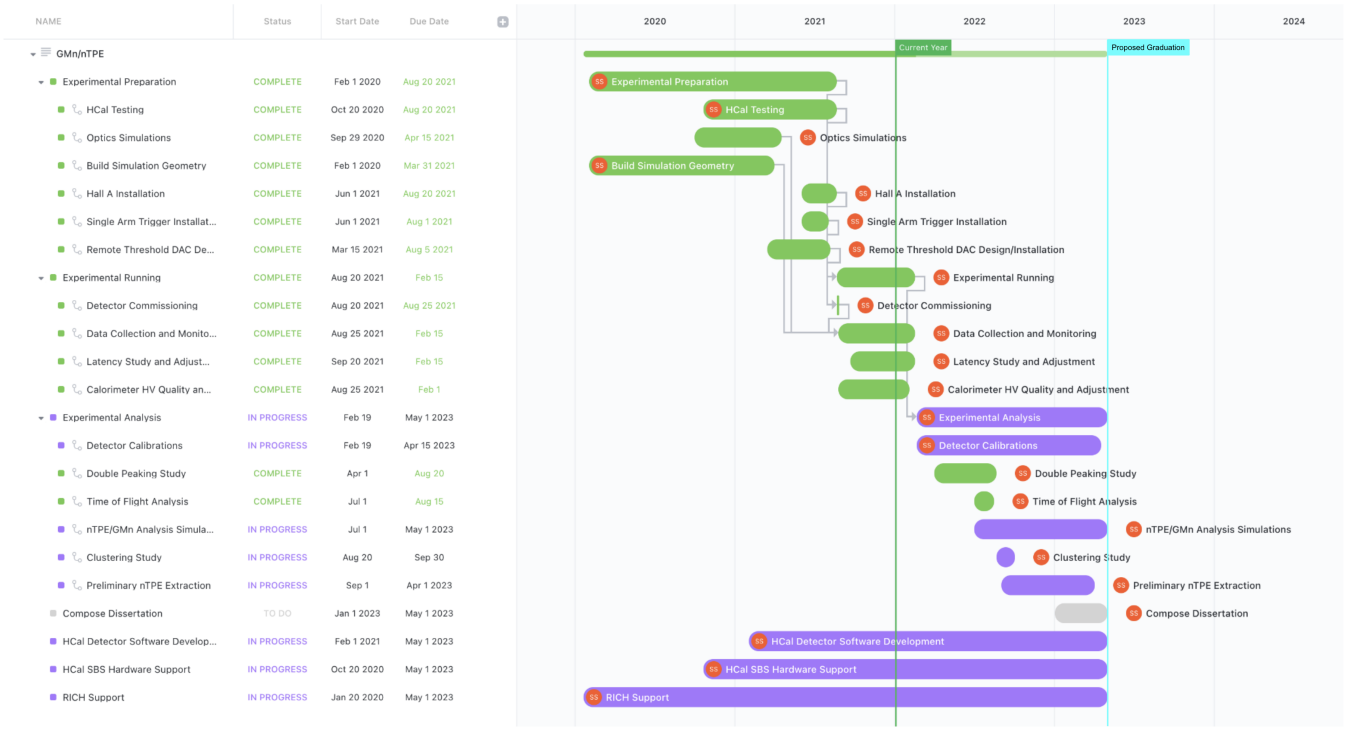

FIG. 15. Proposed PhD Timeline and Roadmap to Dissertation Defense

B. Software

The full list of all software projects can be found on my github:

- https://github.com/sebastianseeds

Among the many forked repositories, $SBS\_offline$ (JLab fork), $hcal$, $HCal\_replay$, and $GMn\_analysis$ are the primary sources of my original work. They include scripts and modifications that govern timing and energy calibrations for HCal, cosmic data analysis, LED analysis, alpha parameter extraction, PMT quantum efficiency, analysis of F1TDC signals, HV/fADC/F1TDC configuration files, functional data replay platforms, fADC spectral analysis, threshold scans, timewalk analysis, accelerator RF timing, HV scans, HCal timing resolution, HCal position resolution, HCal detection efficiency, GRINCH e' track correlations, elastic parsing, p-n yields, preliminary nTPE extractions, TOF simulations and calculations, G4SBS visualizations, G4SBS geometry (several experiments), Panguin online monitoring, ADC waveform and clustering displays, LH2 proton displays (for commissioning), and others.

C. Service

During experimental running for GMn and nTPE, I was the primary on call subject matter expert (SME) for HCal and sieve plate installation entailing software development and controlled and restricted access to the experimental hall for any and all hardware related diagnoses, repairs, and maintenance. I managed the data integrity and monitoring for HCal, verifying that usable signals were being collected and responding immediately to data loss events and anomalies. I was also responsible for calibration of BBCal for several weeks in order to correct for SBS magnet fringe field effects on the BBCal single arm trigger and made multiple controlled accesses into the hall to power cycle subsystem HV crates and replace radiation damaged raspberry pi controllers. Also of note I have presented, or will present, my work to the broader scientific community at DNP, APS April meeting, NNPSS, HUGS, the JLab Hall A/C Collaboration Meeting, JLUO, and at UConn.

D. Other Work

Pursuant to support for later experiments in the SBS run group, along with Provakar Datta, I've characterized the quantum efficiency for over 2000 PMTs at UConn for planned use in the hadron arm Ring Imaging CHerenkov (RICH) detector and packaged all PMTs for transport to JLab. I've also participated in the design for a RICH test stand and will continue to support the development, construction, and characterization of the RICH.

VI. TIMELINE

The next steps towards graduation include primarily continued support for all subsystems and GMn/nTPE data analysis efforts. I expect to have a preliminary result for nTPE before APS April meeting next year which will be included in my dissertation, but additional analysis work to better handle the systematic error and then to publish results will likely continue beyond my graduation date. The proposed timeline for graduation which meets the yearly progress report expectations can be found in Figure 15.

[1] R. Hofstadter *Electron Scattering and Nuclear Structure.* Rev. Mod. Phys. 28, 214 (1956).

[2] M.N. Rosenbluth *High Energy Elastic Scattering of Electrons on Protons.* Phys. Rev. 79, 615 (1950).

[3] J. Arrington, P. G. Blunden, and W. Melnitchouk *Review of two-photon exchange in electron scattering.* Prog. Part. Nucl. Phys. 66, 782 (2011), arXiv:1105.0951 [nucl-th].

[4] P. G. Blunden *Overview of recent theoretical work on two-photon exchange.* AIP Conference Proceedings 1970, 020003 (2018); link

[5] A. Camsonne et al. *Measurement of the Neutron Electromagnetic Form Factor Ratio GEn/GMn at High* Q^2 From Jefferson Lab PAC 34

[6] F.Benmokhtar et al. *Precision Measurement of the Neutron Magnetic Form Factor up to* $Q^2 = 18.0\,(\mathrm{GeV/c})^2$ From Jefferson Lab PAC 34; Program Advisory Committee

[7] Tiefenback, Michael *JLab Accelerator Overview* From CLAS Collaboration Meeting, Jefferson Lab, 2016. link

[8] Liyanage, Nilanga *GEM Detectors for SuperBigbite* From SBS DOE Review, 2018. link